ALEPH 91-70
PHYSIC 91-63
S. Brandt et al.
28.5.1991

Measurements of the absolute luminosity with the ALEPH detector

F. Bird S.Brandt C.Grupen G.Gillessen J.D.Hansen
J.R.Hansen P.H.Hansen J.Harton H.Heiter H.Meinhard
L.Mirabito R.Møllerud B.Pietrzyk U.Schäfer H.Seywerd
C.Stupperich H.Trier J.Wear V.Zeuner

May 27, 1991

Abstract

We report on the luminosity measurement performed with the ALEPH detector at LEP. The systematic errors of the measurements in 1990 are estimated to 0.6% (experimental) and 0.3% (theoretical). A shorter version of this will be submitted to Zeitschrift.

1 Introduction

Precise measurements of the Z cross–section at LEP provide a powerful test of the standard model. At the Z resonance peak, we have:

$$N_\nu \cdot \frac{\Gamma_{\nu\nu}}{\Gamma_{l^+l^-}} = \frac{1}{M_z} \cdot \sqrt{\frac{36 \cdot \pi \cdot f(M_z,\Gamma_z) \cdot L}{N_L} - \frac{3 \cdot N_q}{N_L}} - 3$$

where N_q and N_L are the number of hadron- and charged lepton events, both corrected for acceptance, L is the luminosity and $f(M_z,\Gamma_z)$ is a function [1] which takes into account higher order corrections to the lineshape. Using this expression one can determine N_ν, the number of neutrino species, or alternatively $\Gamma_{l^+l^-}$, the leptonic width. It follows from the expression that the systematic error on the luminosity quickly becomes the dominating error.

The luminosity is measured by comparing the measured rate of Bhabha scattering with the rate predicted by QED. In the QED calculation it is important to include as many terms as possible beyond the Born approximation as well as electroweak effects. Since the cross-section falls rapidly with increasing scattering angle, it is furthermore important to accurately define the smallest scattering angle of the experimental acceptance. In general, one aims at counting Bhabha events in an acceptance for which the predicted rate has the smallest possible uncertainty combining statistical and systematic errors.

We describe in the following sections the apparatus used for the luminosity measurement in the ALEPH experiment. Then we discuss the method used to determine the luminosity and the errors on the basis of data taken during 1990.

2 The Apparatus

The ALEPH luminosity detector is an electromagnetic calorimeter with a track detector in front. Technical details on the mechanical design and construction are described in detail elsewhere [2]. We repeat here only what is needed for the understanding of the luminosity determination, especially concerning the control of the internal geometry of the detector.

The calorimeter (LCAL) is a lead/proportional wire sampling device of nominal thickness 24.6 radiation lengths. It is placed around the beam pipe on both sides of the interaction region; the first sampling layer at a distance 266.8 cm from the nominal interaction point. The calorimeter partly covers a polar angle range relative to the beam from 45 mrad to 145 mrad.

The Small Angle TRack detector (SATR) consists of nine layer of drift tubes arranged in a staggered octagonal configuration, mounted on the front plate of the LCAL. Its front face begins at 245.5 cm from the interaction point. It covers polar angles from 41 mrad to 90 mrad.

2.1 The Luminosity CALorimeter

The calorimeter is mechanically subdivided into four semi-cylindrical modules, each enclosed in their own vacuumtight vessel. Each module has a hole cut out for the beam pipe. The outer radius is 52 cm and the inner radius is 10 cm. The depth of a module is 45 cm. A pair of modules is joined together on each side of the interaction region resulting in a dead zone in the vertical plane of 4 cm width. Except for geometry, the modules are almost identical to those of the electromagnetic calorimeter, ECAL [2].

The electromagnetic showers are sampled both on the anode and on the cathode of the shower detector sampling planes. The anodes are 20 μm thick gold plated tungsten wires strung vertically inside extruded aluminum profiles with 5 mm wall spacing. They are held by wire supports such that the free length never exceeds 38.6 cm. The cathodes are planes segmented into quadratical pads, with a size varying from 28.575 mm to 31.750 mm. These pads are internally connected to form towers pointing to the interaction point. Each tower is segmented into three longitudinal compartments (called 'storeys') corresponding to the first 4.77, the middle 10.6 and the last 9.25 radiation lengths.

There are a total of 38 sampling layers, 9 in the first storey, 20 in the second and 9 in the third. The lead sampling thickness is 2.8 mm in the first two storeys, and 5.6 mm in the third storey. In addition to the analog signals from each tower storey, an analog signal is available from each of the 38 wire planes and from the sum of the planes.

From the anode wire signals the shower energy and the longitudinal shower profile are measured, but no lateral information. The pad readout provides an energy

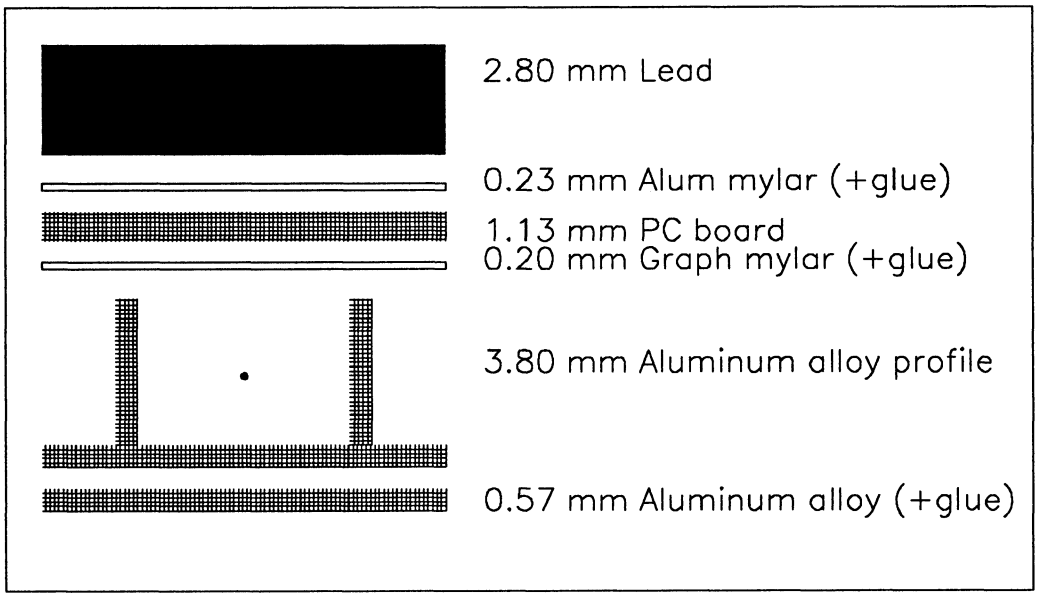

Figure 1: Longitudinal section through a layer.

measurement, a measurement of the lateral profile from which the shower centroid is reconstructed and a rough longitudinal profile.

The modules are built on a 40 mm thick aluminium front plate which supports both the calorimeter and the luminosity track detector. The sampling layers are positioned by two 40 mm diameter bronze dowels passing through precision holes (80 μm larger than the dowels) in the layers and in the front and end plates.

The extrusions and the printed circuit boards (PCB's) anchoring the wires are mounted on a 0.5 mm aluminium sheet. Figure 1 shows details of a single layer. In the following subsections those features of the detector are described which are important for a precise determination of the luminosity.

2.1.1 Active Area

The active area, shown in Fig. 2, starts 2 mm inside the detector from the wire supports in the vertical y–direction. In the horizontal x–direction it is defined by the last ribs of the aluminium extrusions. The cathode pads and the lead layers extend beyond this area so that particles will always enter the active area through lead. The internal wire supports make 3 mm wide dead horizontal zones which are staggered from plane to plane, so as to avoid complete shadowing.

2.1.2 Cathode pad layout

The cathode pad pattern is chess–board like with square pads varying in 6 different sizes from 28.575 mm in layer 1 to 31.750 mm in layer 38. Some pads along the outer perimeter have irregular shapes. For reasons of economy, 5 to 7 identical pad boards follow each other in depth. This means that the boundaries of the individual layers oscillate around a common projective boundary. The amplitude varies with polar angle; at the fiducial boundary of the event selection it is 1.4 mm, which is small compared to the typical shower width of 13 mm.

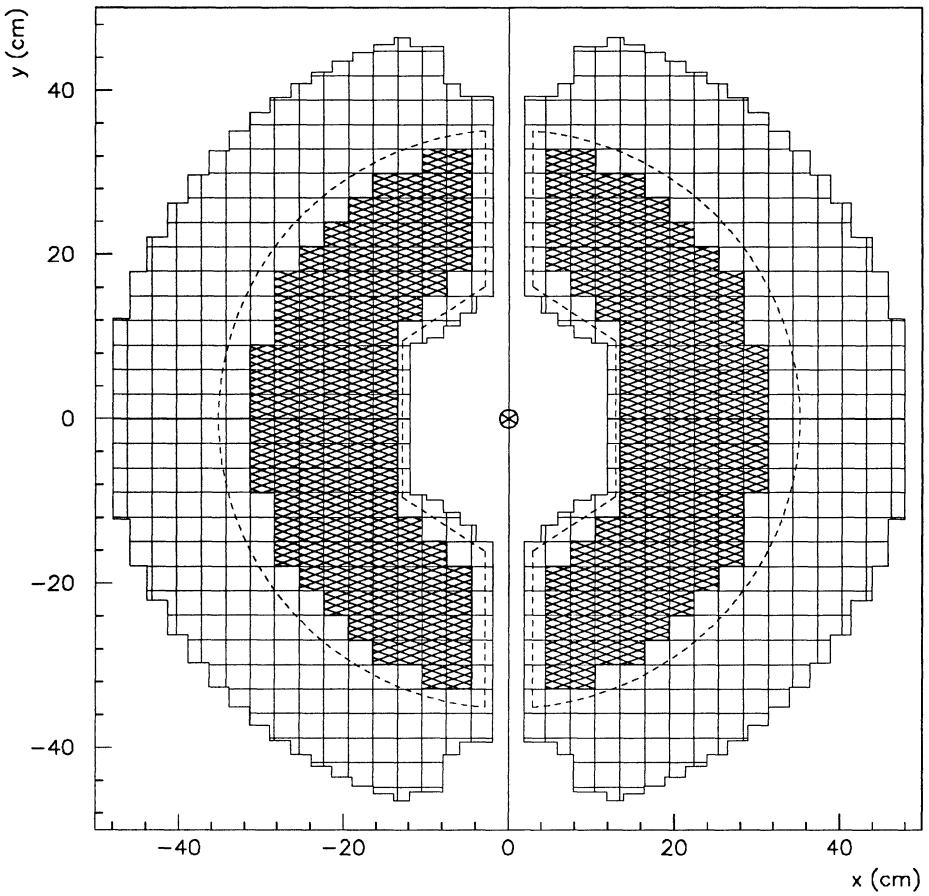

Figure 2: The active area, fiducial region (hatched) and non–fiducial boundary (dashed) of a LCAL module pair. The tower layout is drawn at $z = 280$ cm.

2.1.3 Survey of cathode pad positions

Critical for the luminosity determination is the knowledge of the position of the acceptance regions. Hence the precision of the construction and mounting is very important. The relevant tolerances are shown in Table 1.

The PCB's of a given size is made from a common print such that the error on the relative positions of the cathode pads inside a layer is 50 μm. It is likely that this error is common for all boards of that size, and, since most of the energy is deposited in a limited number of planes, the 50 μm is taken to be the error on any distance between tower boundaries. The position of the PCB layers is fixed by means of steering pins through precision holes drilled in the PCB and the lead sheets, each with a tolerance of 50 μm. The support holes in the lead sheets are positioned with respect to the dowels which carry the stack with a precision of 40 μm. These four uncertainties are common to all modules, while the remaining errors are individual to each module.

The positions of the mounting holes for the dowels in the front and end plate are known with respect to reference marks on the plates with errors given in Table 1. Each pair of modules are supported at the top and bottom by legs connected to the TPC [2]. The legs are equipped with a horizonthal supporting bar connecting the two modules at the front, and the distance between the dowel holes in this bar contributes an error of 60 μm to Table 1. The distance between the two modules may furthermore vary with depth. This opening angle is determined by survey, and checked by comparing positions of SATR tracks with LCAL clusters as discussed in section 7.

The alignment constants are based on a survey. The survey was repeated at four

Relative position of pads	50 μm
Pads to PCB holes	50 μm
PCB holes to lead holes	50 μm
Lead holes to dowel holes	50 μm
Dowel holes to dowels	40 μm
Dowels to supporting holes	40 μm
Supporting holes to front reference marks	100 μm
Front reference marks to center of supporting bar	60 μm
Opening angle error	100 μm
Position error per module relative to center of support bar	190 μm
Average error relative to center of support bar	134 μm

Table 1: Construction and survey errors

different times during 1990, each time providing measurements of three to four points on each module. A comparison of the surveys shows that the center position of each pair is determined with a precision of 0.32 mm in the radial direction and 0.85 mm in z. The internal consistency of the measured points in the surveys indicate an "opening angle" error at the depth of 17.5 cm of 0.10 mm.

Combining the errors in quadrature gives an error of 0.190 mm for each module. When reducing the module independent errors by a factor $\sqrt{4}$, the average error becomes 0.134 mm.

2.1.4 Energy calibration

In order to maintain the energy calibration the following steps are taken:

- The pedestal of each electronic channel is measured and updated regularly using clock-triggered events. This pedestal is subtracted before read-out.
- Towers with less than 10 ADC counts above the pedestal value in all three storeys are suppressed from the read-out. However, the first towers in a group of 32 belonging to the same electronic circuit are not zero-suppressed. The energy of the unsuppressed towers, in events with no anode energy, is used offline to continuosly update the pedestal of the 32 channels.
- A calibration factor which depends on run and module number is determined from selected e^+e^- events. Typical values for the calibration factor are 4.8 MeV/count for storeys and 0.3 MeV/count for wire planes. The precision is limited by statistics to about 0.5%. The factor was stable within 1% , except for a two-week period where a gas leak occured.
- No channel dependent calibration of the gains were applied. Fig. 3 shows that the channel-to-channel variations are 1.4% over the acceptance used. Each channel enters into the plot the observed average energy divided by the Monte Carlo expectation in which the gain is assumed constant.

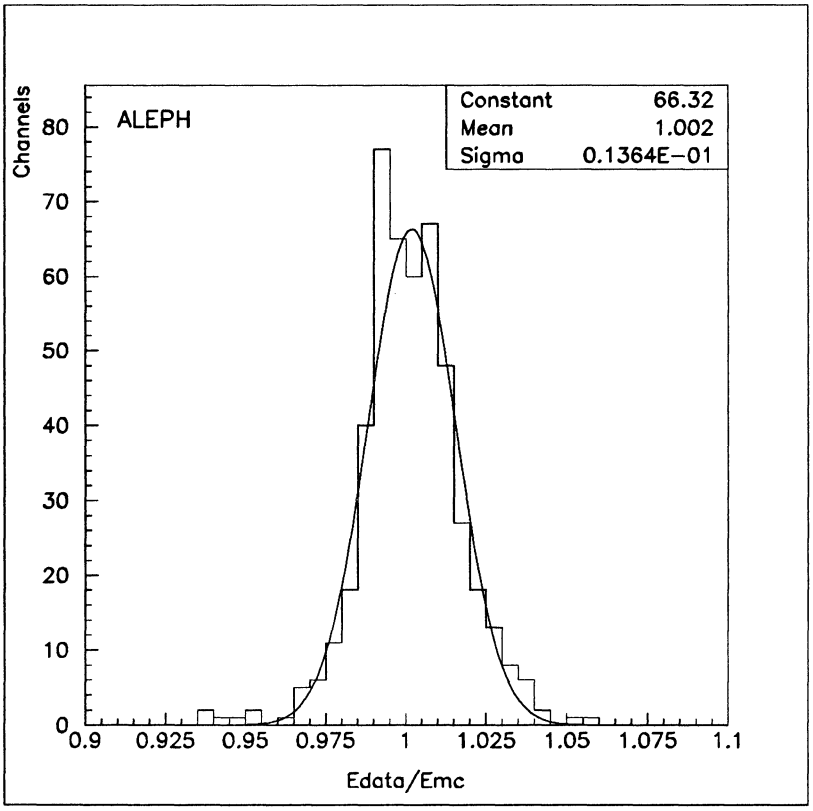

Figure 3: Distribution of ADC channel gains normalized to the expected gain

2.2 The Small Angle TRacker

The complete tracking device [2] consists of thirty-six half planes of drift tube chambers which are arranged in four detectors, two on each side of the interaction point. The center planes are at a distance of 254 cm. One half-plane is made of four 45° sectors, each of which contains 14 drift-tubes. The nine half-planes of one detector are rotated by 15° with respect to one another to avoid dead zones. Because of the 45° modularity of the sectors, there are three sets of planes with different orientation. Planes within one set (i.e. numbers 1,4,7; 2,5,8; and 3,6,9) have the same position in azimuth.

The individual drift cells forming one 45° sector are made from brass tubes with a square cross-section of $9.95 \times 9.95\ mm^2$ outer dimension and a wall thickness of 300 μm. The positioning of the 25 μm anode wires is guaranteed to a precision of 60 μm by notches cut in precision epoxy supports. Individual drift tubes as detector elements were chosen to fight the anticipated high background due to synchrotron radiation at LEP which would have caused serious problems for track reconstruction if low density material drift chambers without separating walls had been used instead.

The amount of material in front of the SATR varies between 14 % and 7.3 % of a radiation length in the angular range from 40 to 90 mrad. The amount of material in the tracker itself represents 67 % of a radiation length.

2.2.1 Performance

The detector is operated with a gas mixture of Ar (90 %) + CO_2 (10 %) and 1 % isopropanol. The stability of the gas gain of the tubes is monitored with the help of an extra drift cell operated in the SATR gas circulation system and irradiated with

5.9 keV photons from an Fe 55 source. The spatial resolution for electron of the single drift cell was found to be (900 ± 100) μm, leading to an rms error on the track polar angle of 0.25 mrad. Accordingly, the azimuthal resolution of the entire chamber was found to be about 25 mrad. These values correspond to an rms of the fitted track position of 640 μm in the radial direction and 3 mm in azimuth.

The single tube detection efficiency is 99.8 % and the overall track reconstruction efficiency – slightly depending on background conditions – amounts to (92.0 ± 0.3) %.

The SATR was surveyed together with the LCAL, and the alignment was checked with Bhabha events. The uncertainty in the inner radius of the SATR acceptance of 0.1 mm contributes an error of 0.4% to the luminosity determined with SATR alone as described in section 8. Due to the proximity of the SATR to the beam pipe and its robustness, it is used at the same time as backgound monitor and has served to optimize the beam conditions at the interaction point.

3 Triggers

Several triggers, based on the analog sum of pulse heights in the towers or wires, are used in the luminosity determination:

1. A coincidence between the electron and the positron sides with more than 22 GeV on one and 10 GeV on the other side using the tower (cathode) signals. Trigger energies in towers are required to be contained within an azimuthal wedge of 60^0.

2. A coincidence of both sides having more than 10 GeV and the energy sum above 45 GeV, all measured with the wire planes (anode) signals.

3. A single arm tower energy exceeding 10 GeV (low), 22 GeV (medium) or 35 GeV (high). These triggers are prescaled.

4. A single arm wire energy exceeding 35 GeV (prescaled).

5. A total wire energy exceeding 35 GeV (prescaled).

6. A prescaled trigger requiring eight fired SATR wire planes in opposite modules in z and ϕ. It is vetoed by the presence of one or more ITC [2] trigger bits, to eliminate events with wide angle tracks.

The triggers, listed by increasing effective threshold for Bhabha events, are the SATR trigger, the wire trigger, the tower trigger and the very high threshold single arm triggers.

4 Selection of events

A sample of Bhabha events is selected on the basis of calorimeter clusters. These are made by joining towers together for which two storeys, containing more than 50 MeV, share a common side or corner. Towers from different modules are not joined.

The centroid of a cluster is calculated from the nine central towers by weighting the center of each tower with the corresponding energy fraction. It oscillates around

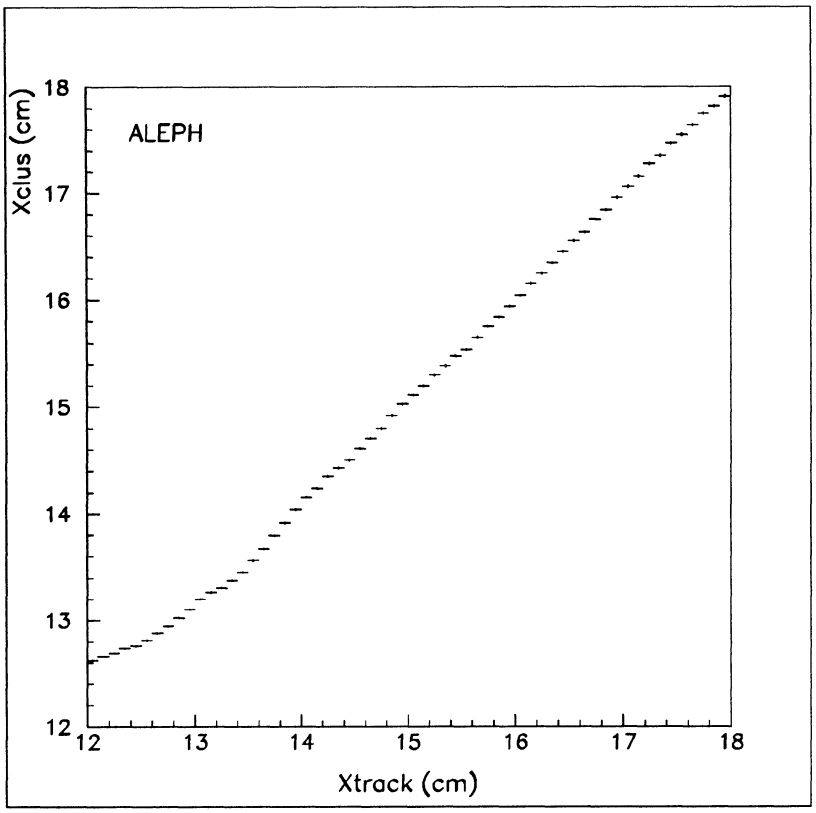

Figure 4: Radial shower position as measured by clusters and tracks.

the true position because of the 3×3 cm tower size. This effect is corrected for using a global function depending on the centroid position within the central tower. Lateral leakage of energy near the calorimeter edge systematically shifts the cluster position into the detector. This shift is not corrected. Fig. 4 shows the coordinate of the cluster versus that of the track near the horizontal plane.

The two clusters with maximum energy, E_1 and E_2, on each side of the interaction region are then required to have the following properties:

- The clusters must be in a certain fiducial region of the calorimeters. A fiducial region is defined on just one side of the interaction region, the choice of side alternating from event to event. The alternation of the fiducial side ensures that the acceptance is independent, to first order, of transverse and longitudinal displacements of the collision point, and of small angular changes of the beam direction. This is shown in Fig. 5 [1].

  The fiducial region follows the boundaries as shown in Fig. 2. It excludes towers along the inner edges of the calorimeters, and also a region at large angles which is in the shadow of material from the central detector. The intersection of the most energetic row and column of three towers must be contained in the fiducial region. Only the energy in the first two storeyes is used in this selection.

[1] A simple geometrical argument shows that the change in counting rate vanishes (to first order) for longitudinal beam displacements $\Delta z/z_0 < \delta/r_0$, where δ is the extra margin on the non fiducial side and r_0 is the inner fiducial radius. For larger displacements the change in counting rate is reduced by δ/r_0 with respect to the case of symmetric cuts

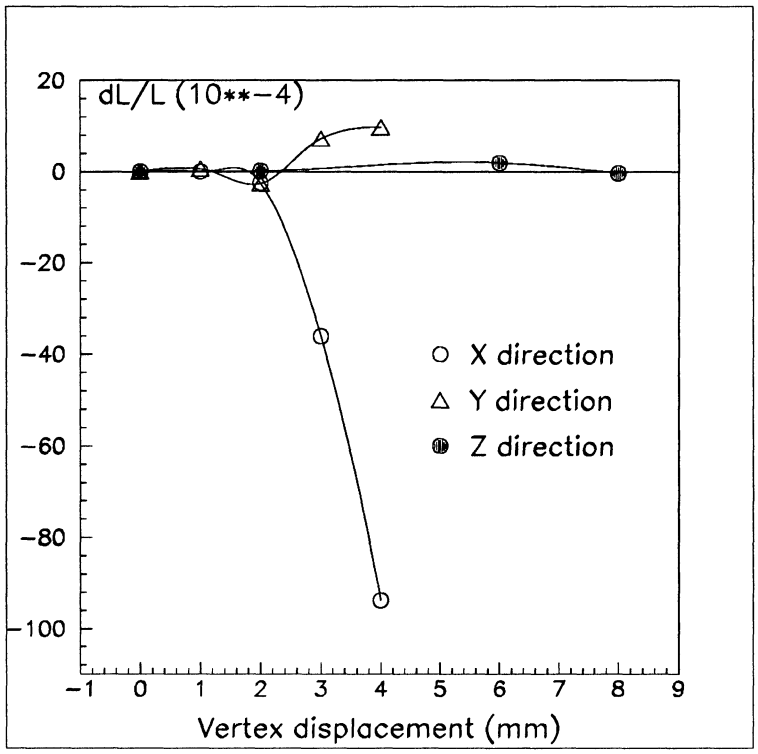

Figure 5: Change in luminosity for different beam dispacements.

On the other side of the interaction region a wider fiducial region is defined using the cluster centroids. This loose fiducial region is defined to be 10 mm inside the edge of the sensitive area of the calorimeter and its outline is also shown in Fig. 2.

The overall agreement between data and Monte Carlo on the geometrical acceptance is illustrated in Fig. 6, showing the distribution of cluster polar angles, and in Fig. 7, showing the distribution of azimuthal angles. An independent view of the acceptance is given by the distribution shown in Fig. 8 of polar angles measured by SATR. Here, the SATRs own acceptance cuts off the distribution at large angles.

- In order to reduce background, the difference in the azimuthal angle between the two cluster centroids is required to be in the interval $170^0 < \Delta\phi < 190^0$. The distribution of this quantity for real and simulated data is shown in Fig. 9. The width of the distribution is mainly caused by fluctuations in the vertex position, and the peak is displaced from 180^0 by the magnetic field (1.5 T in the e^--direction). The excess of data is caused by off-momentum beam particles.

- The distribution of cluster energies and their sum are shown in Figs. 10, 11 and 12. The beam-related background is concentrated at low E_1 and E_2. It is removed by a cut, requiring that both E_1 and E_2 exceed 44% of the beam energy, and that their sum exceeds 60% of the center of mass energy.

  The energy distribution is generally well simulated. The excess of data at high energy comes from overlapping off-momentum beam particles. Below about 40% of the energy, data and simulation are cut off by different thresholds and do not coincide.

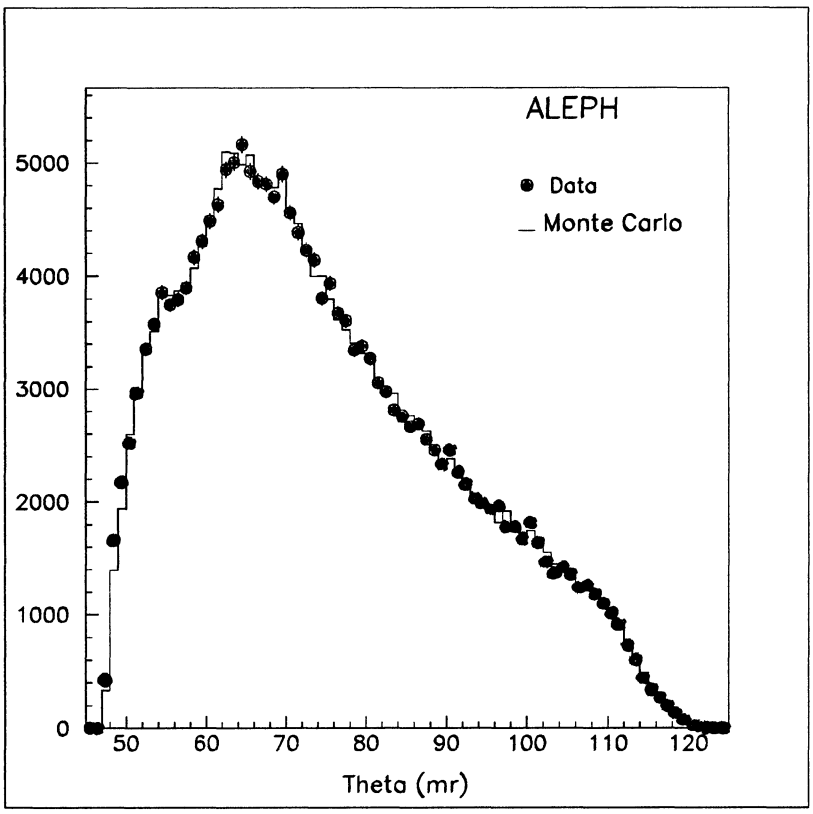

Figure 6: Distribution of the polar angle of accepted clusters on the fiducial side.

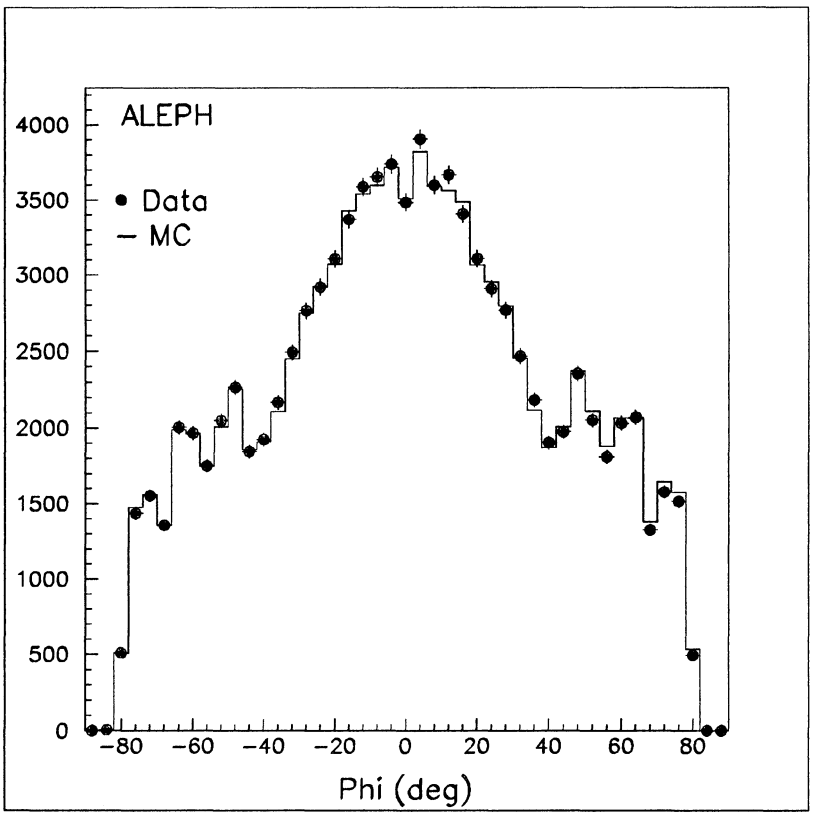

Figure 7: Distribution of the azimuthal angle of accepted clusters on the fiducial side.

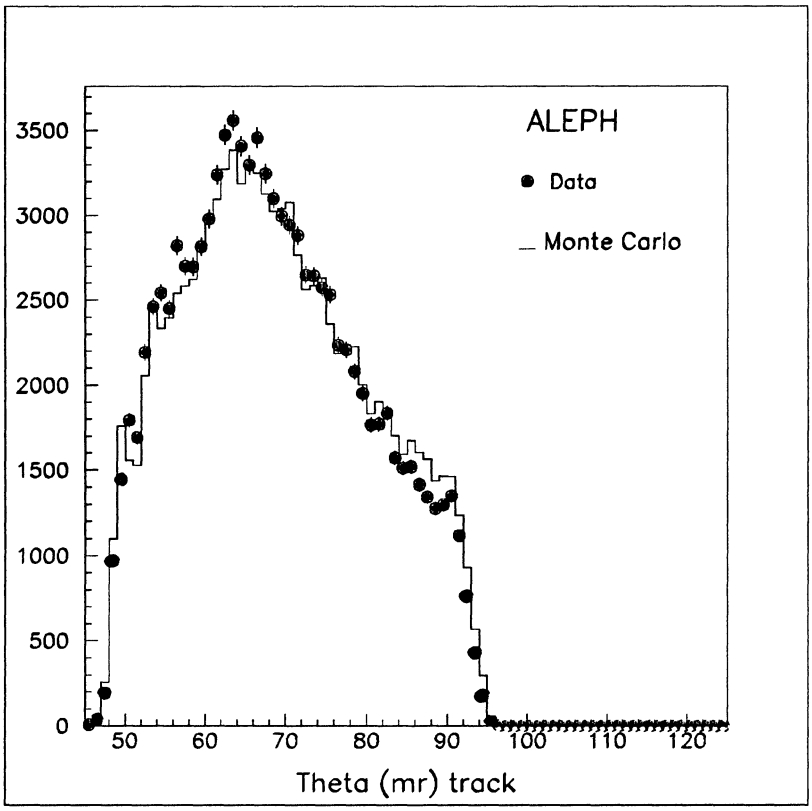

Figure 8: Distribution of the polar angle of accepted tracks on the fiducial side.

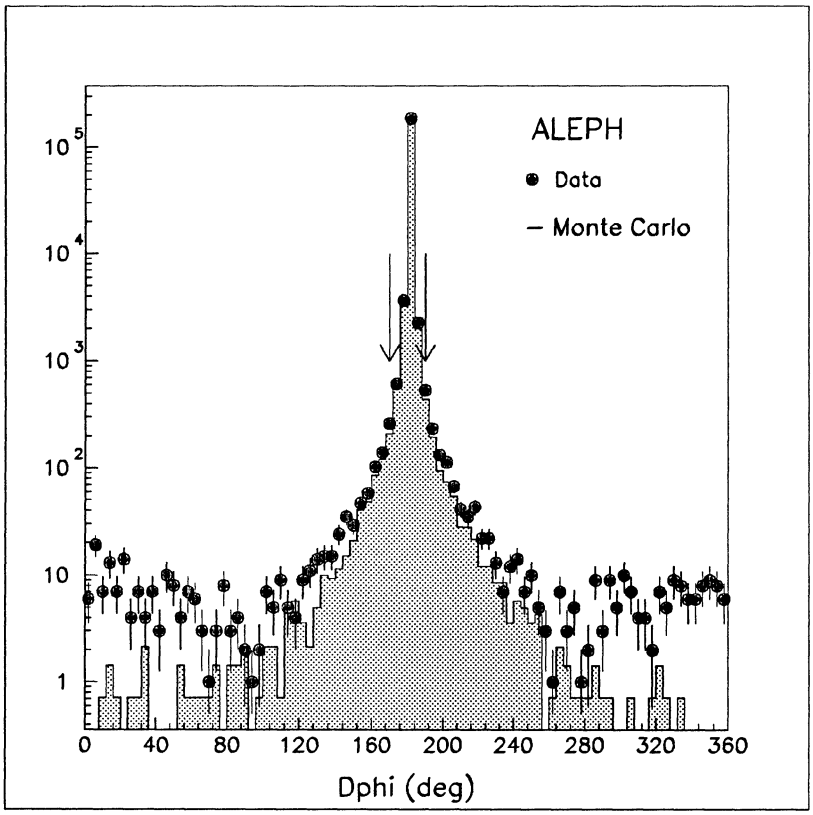

Figure 9: The difference in azimuth, $\Delta\phi$, between the two clusters.

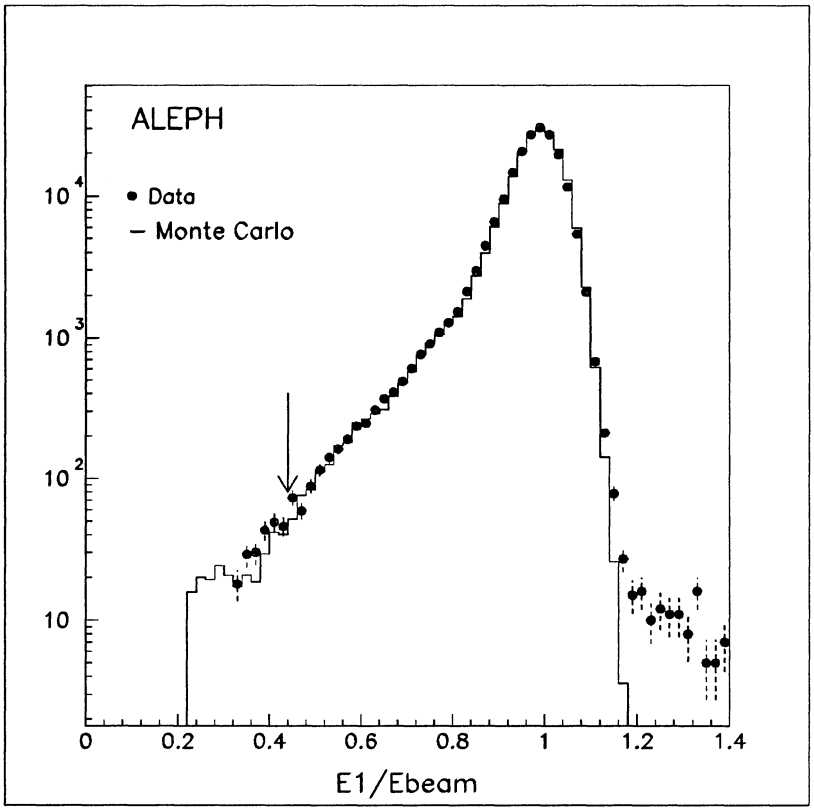

Figure 10: The energy on the fiducial side. The arrow indicates the selection cut.

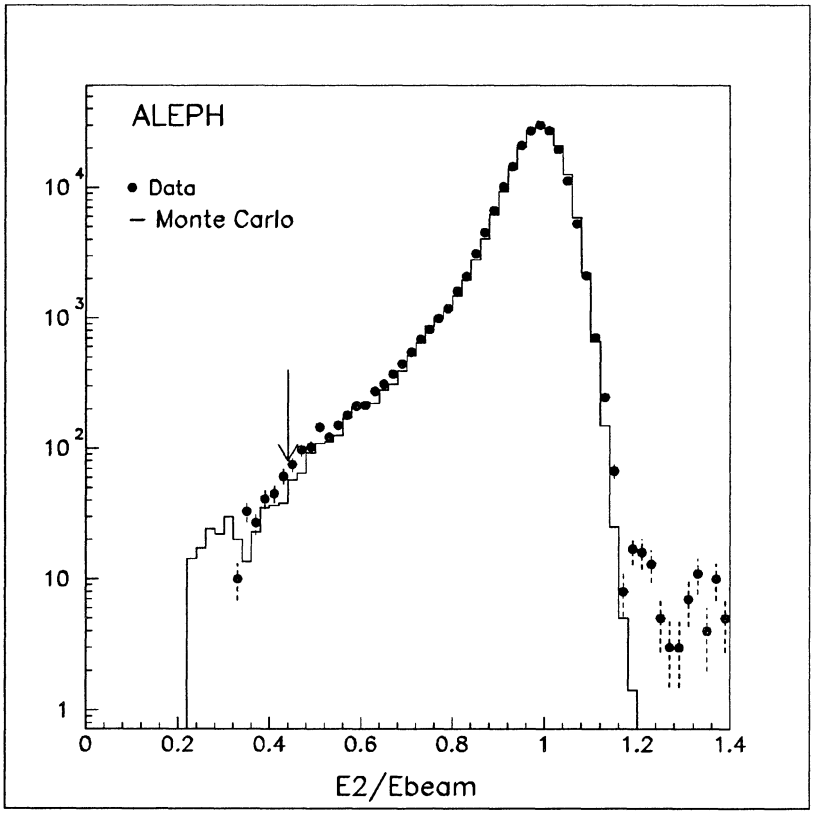

Figure 11: The energy on the non-fiducial side. The arrow indicates the selection cut.

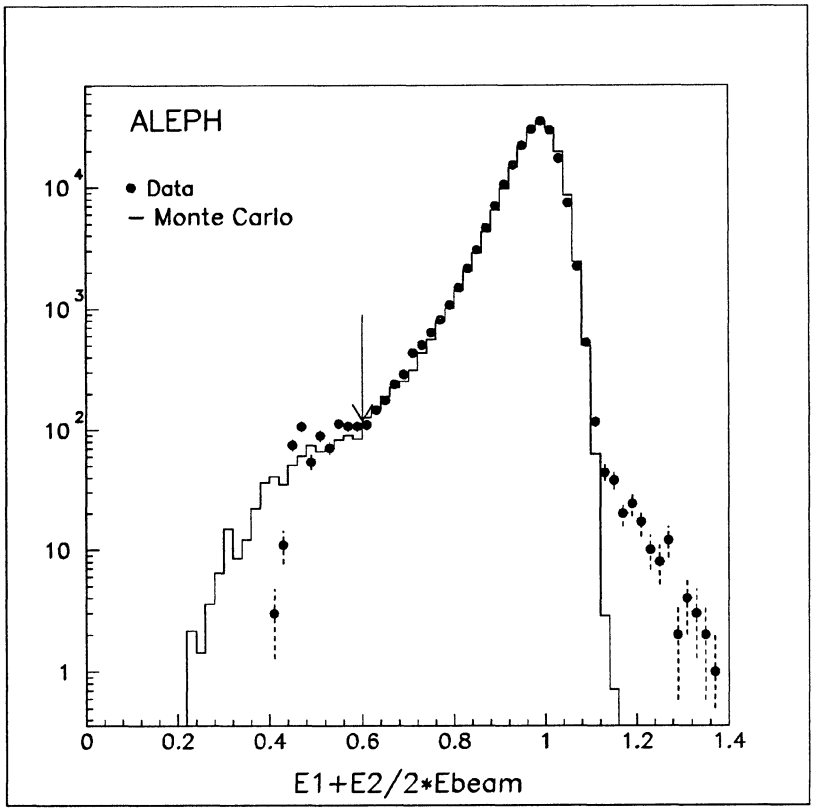

Figure 12: The total energy. The arrow indicates the selection cut.

5 Background

The events are selected so as to eliminate background from off–momentum beam particles. The number of remaining background events in the sample is estimated by the number of events in the interval $0° < \Delta\phi < 10°$. This is a good estimator of the beam–related background, since fake background events constructed from single arm triggers occur with similar frequency in the region $0° < \Delta\phi < 10°$ as in the signal region $170° < \Delta\phi < 180°$ (the ratio is 0.92 ± 0.12). This way a contamination of $0.024\% \pm 0.004\%$ is found.

Genuine non-Bhabha interactions cause very little background. A sample corresponding to 20 pb^{-1} of two–photon collisions has been simulated using both the Born approximation and the vector dominance model. After applying the selection criteria on the simulated events, we find a contamination of $1.4 \cdot 10^{-5}$ [8,7].

The reaction $e^+ + e^- \rightarrow \tau + \bar{\tau}$ where the tau leptons decay into an electron or a neutral pion could contribute. A contamination of $0.4 \cdot 10^{-5}$ is derived from a Monte Carlo sample corresponding to 20 pb^{-1} [8].

The contribution from $q\bar{q}$ events is assumed to be less than the $\tau\bar{\tau}$ contribution. A check on the combined two–photon background and the $q\bar{q}$ background is done by counting accepted events with a track seen in the central detector. Such events constitutes 0.02% of the data. This must be regarded as an upper limit on the background, since converted radiative photons from Bhabha events contribute.

The contribution from annihilation into two hard photons is estimated by Monte Carlo simulation to be 0.07% [6,7,8]. This is reasonably consistent with Fig. 13 in which the $\Delta\phi$ distribution is shown for events with no tracks. Since photons do not

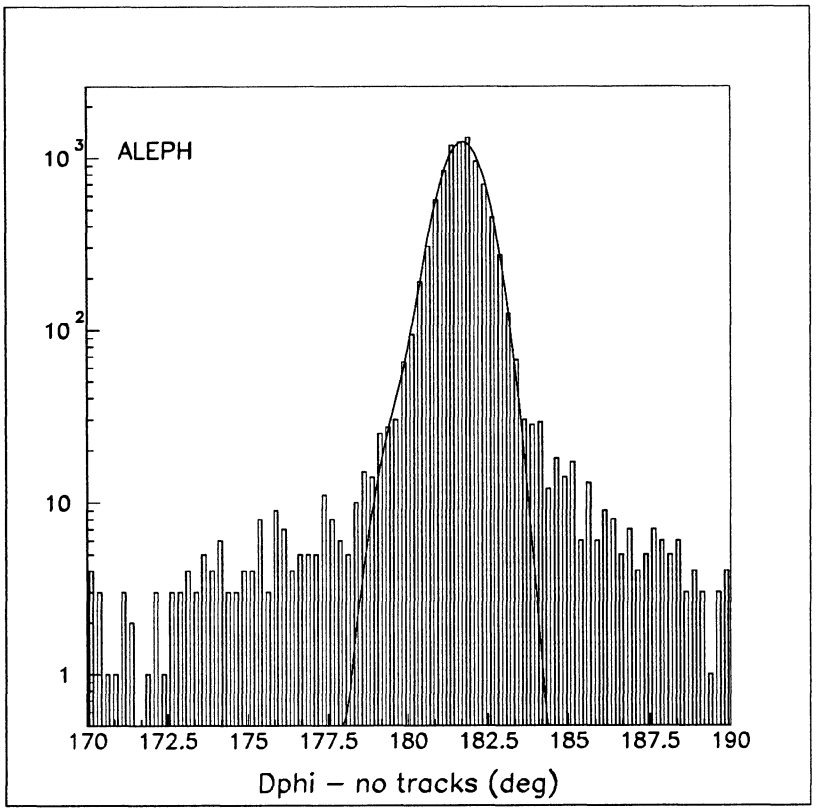

Figure 13: Distribution of the difference in the azimuth, $\Delta\phi$, between two clusters with no track (see text).

suffer magnetic deflection, the photon events should show up as an enhancement near 180°. A fit to the distribution, using two Gaussians with the same width and one of them centered at 180°, prefers a photon contamination of 0.05% ± 0.01% relative to the total sample.

In total we subtract a background contamination of 0.10% ± 0.02 % from the signal.

6 The Bhabha cross section

The luminosity is given by:

$$L = \frac{N_{Bhabha}}{\sigma_{Bhabha}}$$

A reference cross–section, σ_{ref}, at a particular beam energy, is calculated using a generator (BABAMC) for the reaction $e^+e^- \rightarrow e^+e^-(\gamma)$ including first-order radiative corrections [3] and hadronic vacuum polarization [4]. Monte Carlo events are generated at a collision energy of 91.0 GeV and at scattering angles between 15 mrad and $\pi/2$. With the additional input of a Z^0 mass of 91.17 GeV, a 150 GeV top mass and a 250 GeV Higgs mass, the program calculates a Z^0 width, $\Gamma_{z,ref} = 2.475$ GeV. Finally, an infrared cut-off parameter k_0 is set equal to 0.001.

Among the generated events, only those are passed through the detector simulation which contain particles in the active volume of the detector carrying either 10% of the collision energy on each side, or 35% of the energy in total. After digitization by the simulation program, the events are passed through the same analysis chain as the data,

and a cross–section, σ_{ref}, for the event selection is extracted.

The cross–section at other energies squared, s, other Z^0 masses squared, s_z, or other Z^0 widths are found using the formula:

$$\begin{aligned}\sigma &= \sigma_{ref} \cdot \frac{s_{ref}}{s} \\ &\cdot(1 + \frac{b \cdot s \cdot (s - s_z) + c \cdot s^2}{(s - s_z)^2 + s^2 \cdot (\Gamma_z^2 + d)/s_z}) \\ &/(1 + \frac{b \cdot s \cdot (s_{ref} - s_{z,ref}) + c \cdot s_{ref}^2}{(s_{ref} - s_{z,ref})^2 + s_{ref}^2 \cdot (\Gamma_{z,ref}^2 + d)/s_{z,ref}})\end{aligned}$$

The constants, $b = -4.43 \cdot 10^{-4}$, $c = 2.22 \cdot 10^{-6}$ and $d = 1.996$ GeV^2, result from a fit to the cross–section generated at parton level for different energies. The parameter d is introduced to account for the fact that high order terms broadens the Z width. In this way the correction term takes into account the weak interaction effects and the extra energy dependence of the first-order radiative corrections.

The angular distributions of QED events and Z^0 resonance events are different. The constants b and c are proportional to integrals over the angular range with the consequence that the exact values depends on the selection criteria. For example, if the inner boundary is moved into the detector by one tower width, then $b = -4.74 \cdot 10^{-4}$, $c = 2.61 \cdot 10^{-6}$ and $d = 1.83$ GeV^2, which changes the correction factor by very little. All together, the expression is found to describe the energy dependence of the cross–section better than 0.03% at all energies.

The reference cross section, σ_{ref}, for our acceptance is found to be $(26.30 \pm 0.16_{exp} \pm 0.08_{theory})$ nb.

7 Errors in the luminosity determination

The experimental systematic error on the Bhabha cross section results from Monte Carlo statistics and uncertainties in the simulation, calibration and positioning of the calorimeter. The verification of the errors is limited by the statistics of the data (194142 accepted events) and the Monte Carlo simulation (271313 accepted events).

A summary of systematic errors is given in Table 2. The individual contributions are described in the following.

7.1 Trigger errors

Using single arm triggers and assuming that the two sides are independent, the wire triggers alone are found to have an inefficiency of 0.001%, which becomes an upper limit for the trigger inefficiency when including the tower triggers.

From the SATR triggers we can estimate the inefficiency that might arise from a correlated failure of all the LCAL triggers, like a power cut which the monitoring system fails to detect. An upper limit of 0.15% is found for the running period of the SATR triggers, which comprised about 1/3 of the data. In conclusion, we assume no trigger inefficiency and no systematic error from this source.

Background estimate (see sect. 5)	0.0002
Alignment and mechanical tolerances (see sect. 7.2)	0.0024
Beam parameters and overall position (see sect. 7.3)	0.0001
Angular resolution (see sect. 7.4)	0.0001
Fiducial side cut (see sect. 7.5)	0.0040
Loose side cut (see sect. 7.6)	0.0015
$\Delta\phi$ cut (see sect. 7.7)	0.0010
Energy cut (see sect. 7.8)	0.0023
Approximation of energy dependence (see sect. 6)	0.0003
Statistics of simulation (see sect. 7.9)	0.0019
Total experimental uncertainty	0.006

Table 2: Summary of experimental systematic errors in the luminosity measurement. Values listed are fractions of the luminosity.

7.2 Relative position of the fiducial region

The position of the fiducial regions relative to the center of a pair of modules determines the inner radius of the acceptance and thus strongly influences the Bhabha counting rate. We use the SATR to check whether this position is correctly simulated.

Fig. 14 shows the distribution of the difference in the radial impact position measured by LCAL and SATR, while Fig. 15 shows corresponding azimuthal distribution. The events are required to have Θ larger than 60 mrad and the positions are extrapolated to at $z_{ref} = 280$ cm, the plane of the average shower maximum. The average radial displacement of LCAL with respect to SATR is -0.07 mm in the data and -0.16 mm in the Monte Carlo. The agreement is well within the expected position error of 0.16 mm obtained by combining LCAL and SATR tolerances (see Table 1 and section 2.2.1).

In order to check more directly the placement of the fiducial boundary, the accepted fraction of the events is shown in Fig. 16 as a function of the radial coordinate measured by SATR. The events are here confined near the horizontal plane. From a fit to the distribution, we find a difference in the halfheight position between data and Monte Carlo of -0.03 $\pm$ 0.10 mm (where the error comes from changing fit ranges). Fig. 17 shows the same for events selected with another boundary which is moved one tower away from the beam. Here, the difference is -0.19 $\pm$ 0.10 mm, larger than for the standard boundary, but still consistent within the position error of 0.16 mm and the average difference in radial impact position described above. The difference between the two fiducial boundaries is discussed further in section 7.5.

Since the comparisons are affected by errors in positioning and simulation of both LCAL and SATR, as well as statistics, we take as the relative position error the nominal average error of the LCAL inner radius of 0.134 mm from Table 1. An error on the effective inner radius results in a luminosity error given approximately by:

$$\frac{\Delta L}{L} = 2 \cdot \frac{\Delta r_{min}}{r_{min}} \cdot \frac{1}{1 - (\frac{r_{min}}{r_{max}})^2} \qquad (1)$$

where r_{min} = 150 mm is an average minimum radius and r_{max} = 300 mm is an

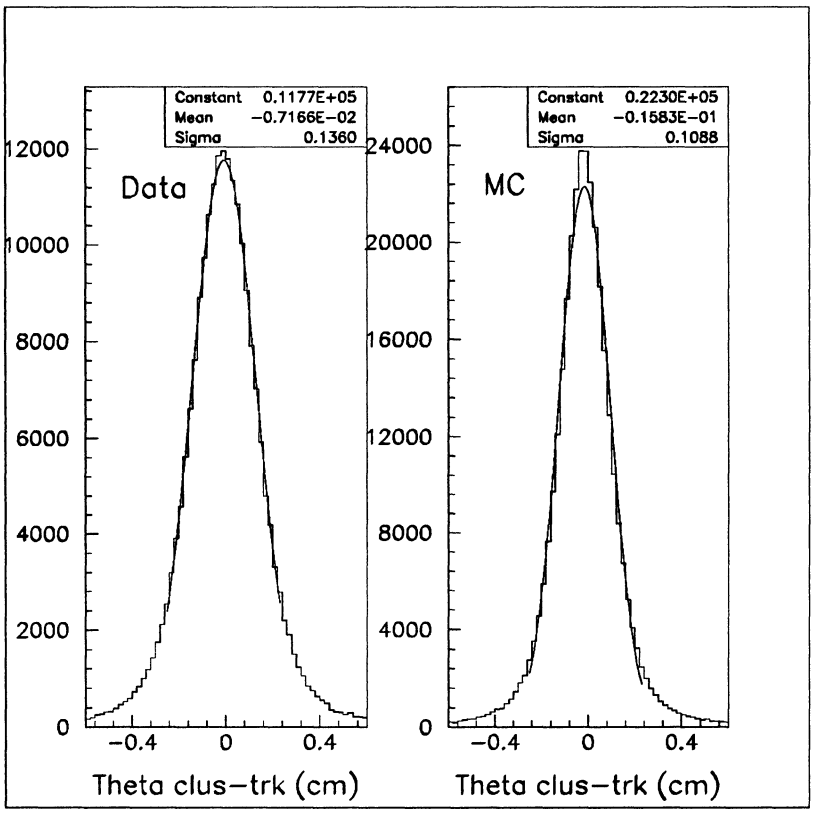

Figure 14: Distribution of difference in polar angle measured by LCAL and SATR

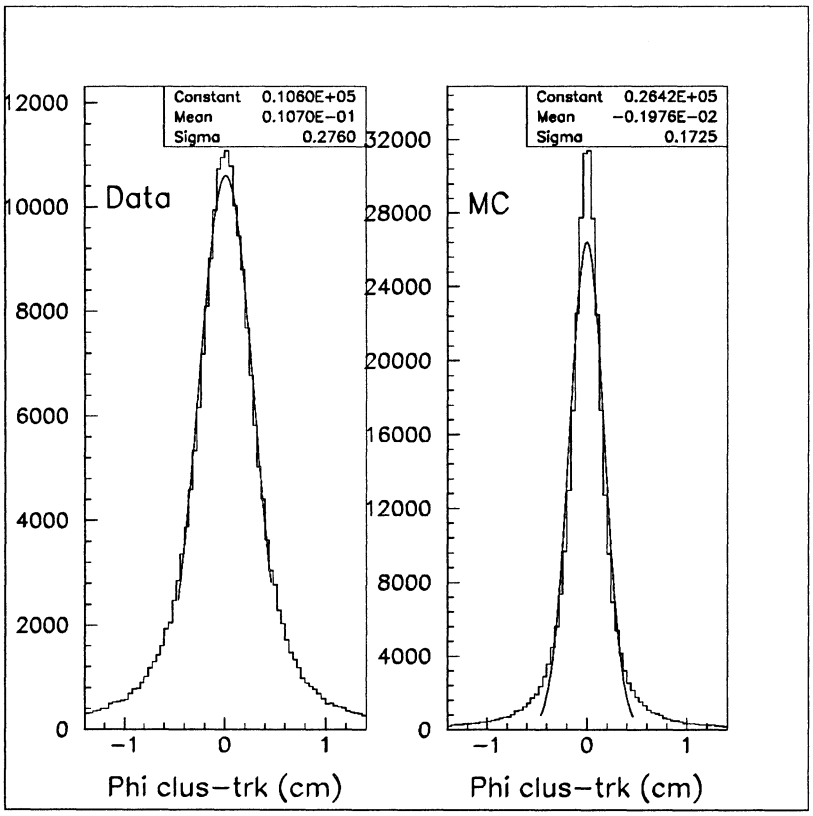

Figure 15: Distribution of difference in azimuthal angle measured by LCAL and SATR

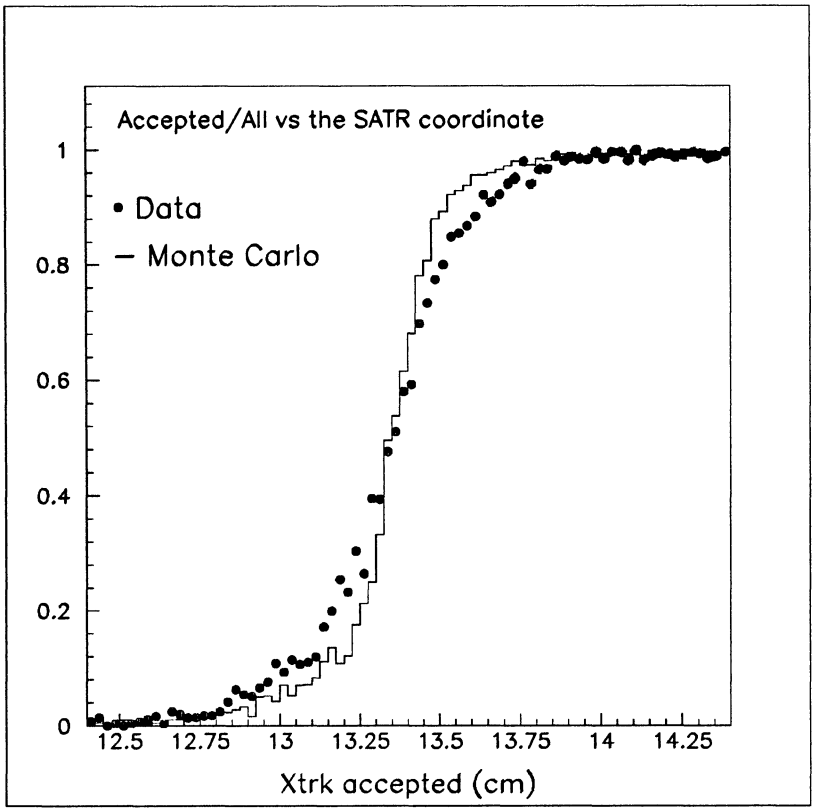

Figure 16: The acceptance of the inner boundary near the horizontal plane as measured by SATR

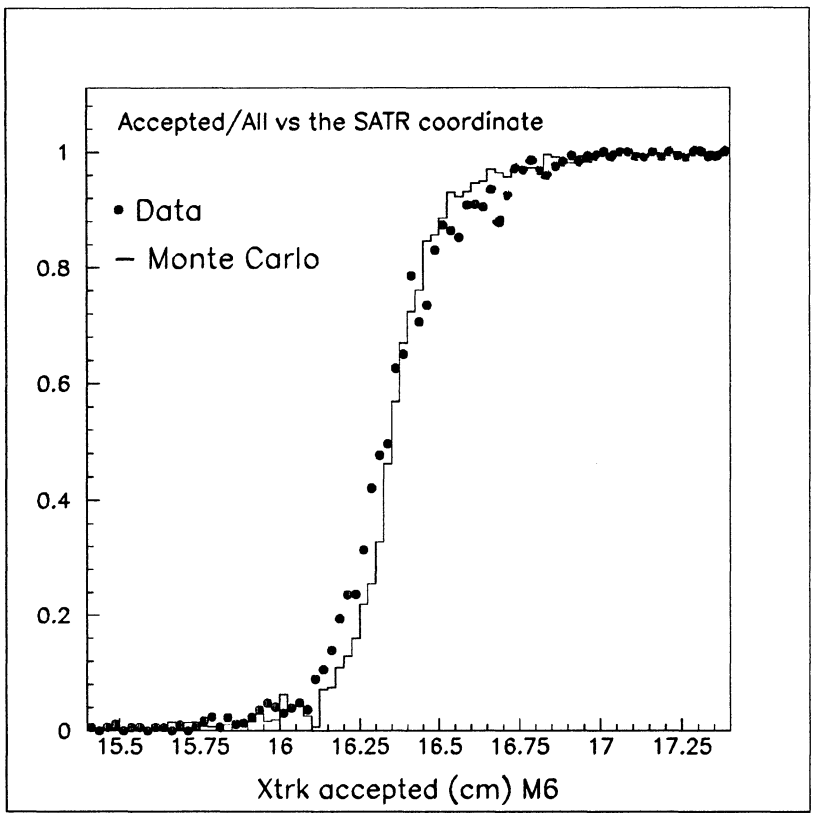

Figure 17: The acceptance of an inner boundary moved one cell into the detector as measured by SATR

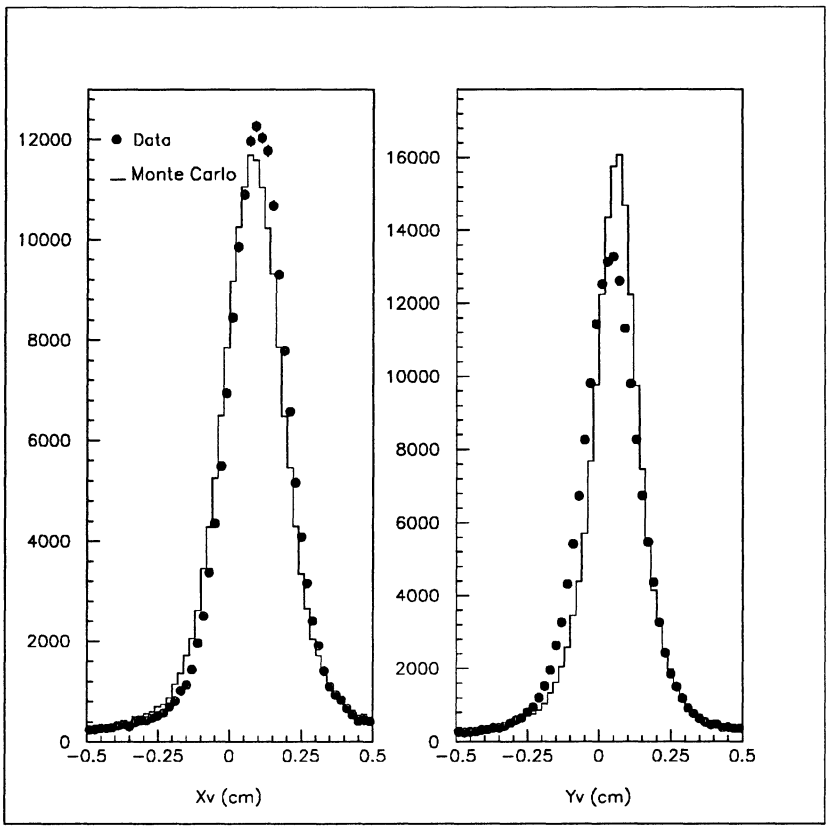

Figure 18: Vertex position at beam crossing as reconstructed from Bhabha events.

average maximum radius. This leads to an error of 0.24%.

7.3 Beam parameters and position of the center of two modules

Moving or tilting the beam is equivalent to a displacement or tilt of the detector. An estimate of the error introduced by small displacements is:

$$\frac{\Delta L}{L} = 2 \cdot (\frac{\Delta r}{r_{min}})^2 \tag{2}$$

where Δr is the displacement of the beam or of the center of two modules.

The effect of beam displacements is shown in more detail using a Monte Carlo simulation in Fig. 5. The actual displacement are shown in Fig. 18, where the transverse beam position is measured using the shower positions and assuming collinear particles. The data and Monte Carlo agrees within 0.2 mm. Since the difference between data and Monte Carlo is the same in both pairs of opposing modules, the longitudinal position must agree within 1mm. The observed displacements include effects of any possible beam tilt. Using Fig. 5 these observations indicate vanishing errors from displacements or tilts. We assign, however, an error of 0.01% from this source.

7.4 Angular resolution

The width of the distribution shown in Fig. 14 is dominated by the experimental resolution of LCAL while SATR dominates the width of Fig. 15. These distributions

are consistent with a 0.25 mrad resolution of SATR and a resolution of LCAL of 0.5 mrad in the radial direction.

An error in the simulated resolution, σ, changes the luminosity by roughly:

$$\frac{\Delta L}{L} = 3 \cdot \frac{\Delta \sigma^2}{r_{min}^2} \tag{3}$$

An error in the beam position spread or divergence contributes in the same manner. Using $\Delta\sigma^2 = 2$ mm^2 and $r_{min} = 150$ mm, we obtain the error of 0.01% in Table 2.

7.5 Fiducial side cut

Errors in material simulation or cell-to-cell calibration could produce a difference in the effective fiducial boundary position. As mentioned earlier, we observe certain discrepancies between data and Monte Carlo when moving the fiducial boundary. The distance of closest approach from the beam to the fiducial boundary has been measured using SATR. For the standard fiducial boundary this distance agrees perfectly in data and Monte Carlo. If, however, the boundary is moved into the detector by one cell, the distance is 163.39 $\pm$ 0.07 mm in data and 163.58 $\pm$ 0.07 mm in Monte Carlo. The latter value is also the one expected for the average cell size of 29.75 mm. If the difference is taken to represent an error in the simulation of the inner radius, then equation 1 predicts that the "real" luminosity minus the standard one is +0.33% $\pm$ 0.17%.

The difference in luminosity between the tighter boundary and the standard one is found to be -0.38 $\pm$ 0.19%. Note, that it has the opposite sign of the difference predicted from the SATR measurements. If also the non-fiducial boundary is moved, the difference with respect to the standard selection varies between -0.25% and -0.40% (see Fig. 22).

We have searched for an explanation for such discrepancies. One possibility is the higher order corrections not included in the generator. Actually, a small shift in the right direction (-0.08 $\pm$ 0.03%, see Table 5) is expected from that source.

Also the simulation of shower shapes is investigated. Fig. 19 compares data and simulation for the transverse cluster size and the energy fractions in the three storeys. The transverse size is taken as the r.m.s. spread of tower centers belonging to the cluster. It is found to be 23.62 mm in the data, and 23.78 mm in the Monte Carlo. A one millimeter difference in the mean value would cause a 0.14% error in the luminosity [7]. Thus, the simulation of the shower width can not be responsible for the effect of changing the acceptance.

Because the towers are not perfectly projective, also the simulation of the longitudinal shower development matters. The standard selection is based on the energy in storey1 and storey2, where storey2 dominates. An event selection on the fiducial side using only storey1 gives a relative change in the number of events of -0.17 $\pm$ 0.02% in the data and -0.30 $\pm$ 0.04% in the Monte Carlo. The change in luminosity is 0.14 $\pm$ 0.05% [8].

Finally, an energy calibration error on the two sides of the fiducial boundary could change its effective radius. The observed cell-to-cell variations along the boundary are found to give rise to a 0.05% error in the luminosity [7].

In conclusion, we have found no particular effect which can explain a -0.4% change in the luminosity when tightening the fiducial boundary, and no indication as to whether

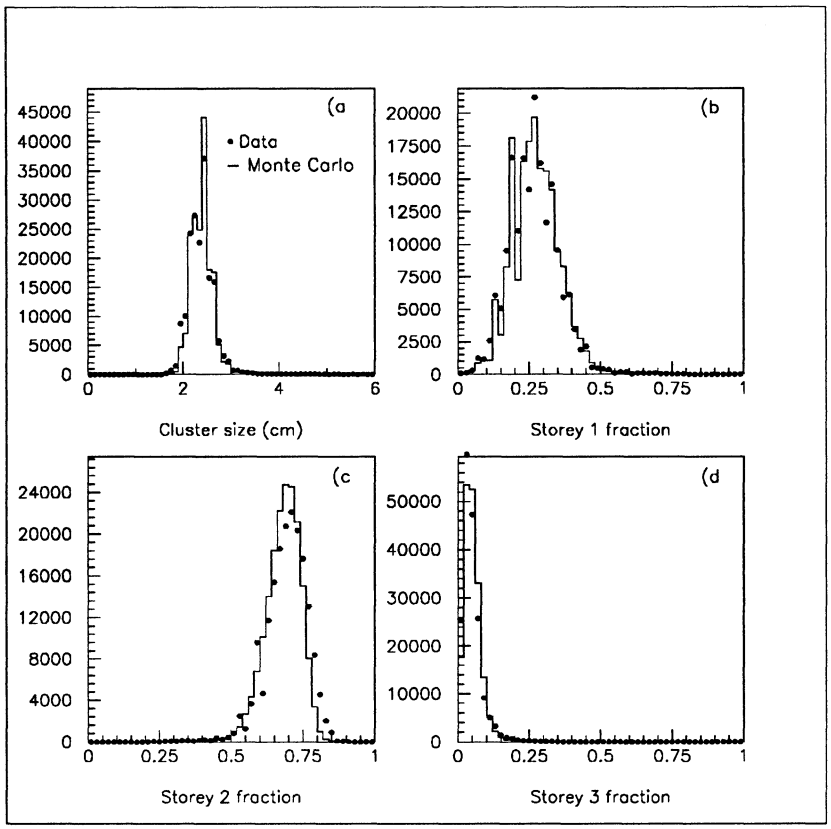

Figure 19: Comparison of shower shape variables. a) the transverse size, b) the energy fraction in Storey1, c) in Storey2 and d) in Storey3.

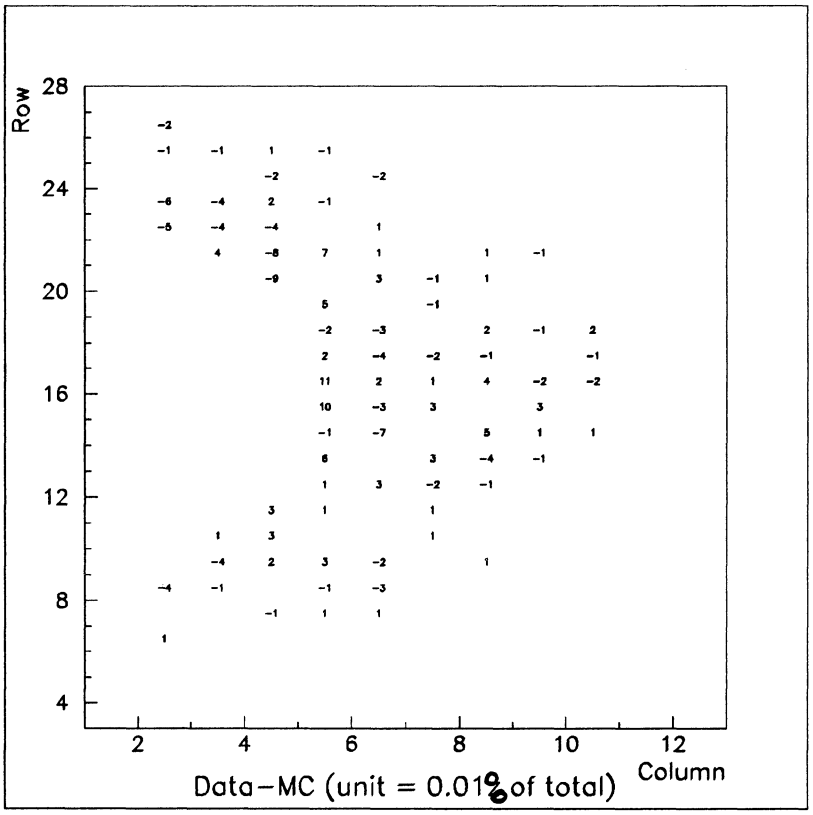

Figure 20: The difference in event counts between data and Monte Carlo in each cell averaged over the four modules.

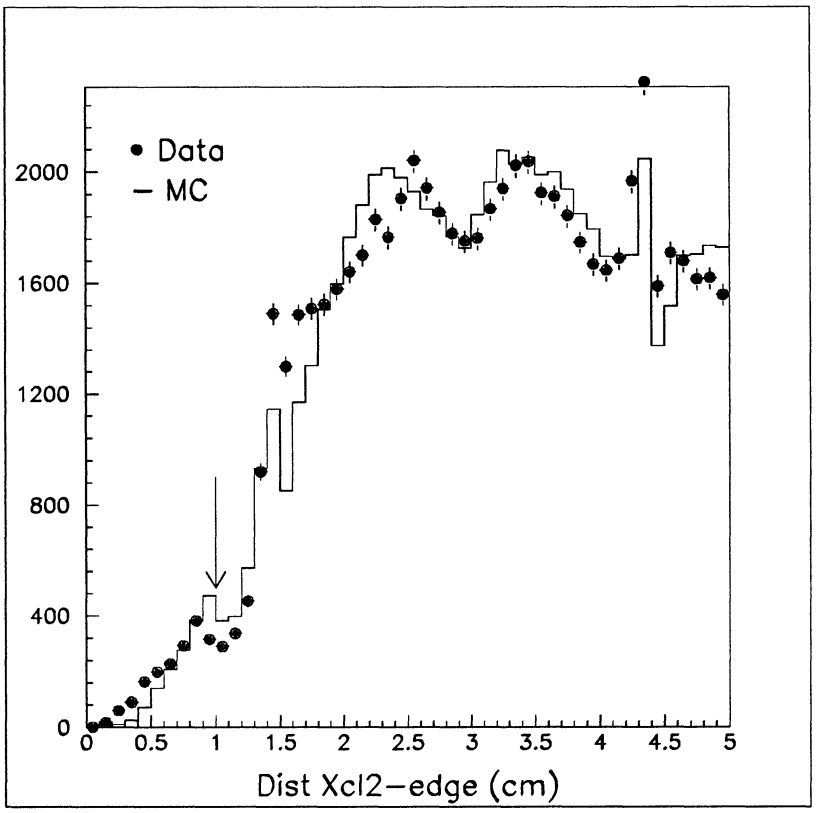

Figure 21: Distribution of the distance to the edge of the detector on the non-fiducial side. The arrow indicates the cut of the event selection.

the tight boundary provides more correct results than the standard one. In Fig. 20 the difference between data and Monte Carlo, after normalising the total accepted Monte Carlo sample to the data, is shown as a function of all cell types. It is seen that it is not possible to define a stricter fiducial region which deviates more than 0.4% from the standard. As a conservative choice for the systematic error on the boundary simulation, we take 0.40%, the largest observed difference due to a variation of the cut (ignoring the compensating higher order correction and the statistical error).

7.6 Loose side cut

Fig. 21 shows the distribution of the distance to the edge of the detector for the side with the loose geometrical cut. Variations of the cut, normally at 10 mm, between 0 and 13 mm change the luminosity by maximally 0.15%. If the loose cut on the outer radius is moved out towards infinity, no change in the luminosity is seen. The error introduced by this cut is therefore set to 0.15%.

7.7 Coplanarity cut

The coplanarity cut on $\Delta\phi$ could cause an unsimulated loss of events due to sudden pedestal shifts which have occasionally happened or due to an overlapping off–momentum beam particle. Such effects could change the cluster ϕ by maximally 20° [8]. When the $\Delta\phi$ cut is relaxed to 150^0, the luminosity increases steadily with respect to nominal by 0.10%, which is taken to be the systematic error from the cut. The

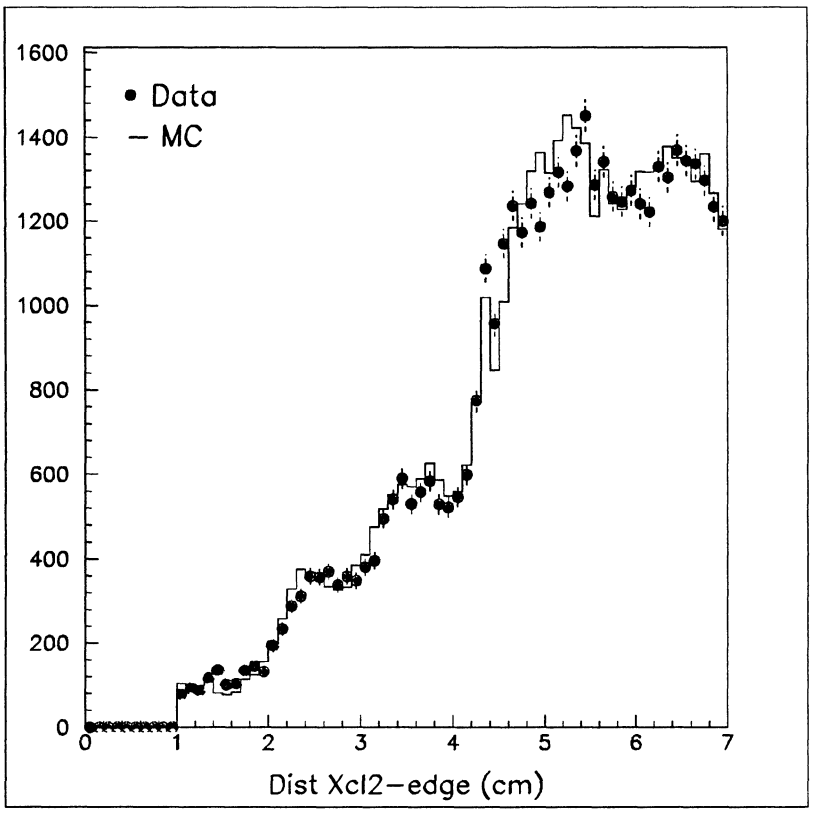

Figure 22: Distribution of the distance to the edge of the detector on the non-fiducial side for the tighter fiducial region

increase in luminosity as a function of the cut could also be partly owing to neglected higher order contributions.

7.8 Error from the Energy Cut

The distribution of cluster energies, for clusters fully contained in the calorimeter, is required to peak at the current beam energy. This fixes the beam energy point on the energy scale to better than 0.1%. A change of the energy cuts by ±5% changes the number of events by ±0.13%. Since the peak position in data and Monte Carlo agree within 0.1%, the error from the global energy scale is negligible.

Non-linearity of the energy response also contributes to the error, if it is not properly described in the Monte Carlo. If the cut on the energy sum is varied from 0.50 to 0.78 of the total energy (the standard cut is at 0.6), and the cut on each leg is simultanously varied from 0.36 to 0.56 of the beam energy (the standard is 0.44), then the luminosity changes steadily by +0.14 ± 0.02% to -0.22 ± 0.04%. An extrapolation of the change down to a cut at zero, assuming a constant ratio between data and Monte Carlo, yields +0.23 %. Again we know of no particular reason for such a discrepancy.

The internal wire supports of the calorimeter could present a risk of unsimulated energy losses. However, if their locations are left out of the luminosity calculation, then it changes by only 0.07 ± 0.12%. Similarly, the support dowels of SATR degrades the energy somewhat. These are placed near cells forming the outer boundary of the fiducial region. Leaving out the entire outer boundary, i.e. reducing its radius by one cell, decreases the luminosity by -0.03 ± 0.06%.

A possible source of the discrepancies is again neglected higer order corrections. We assign a combined error from the energy cuts of 0.23%.

7.9 Statistics of simulation

The Monte Carlo generator calculates a cross section with a relative uncertainty of $\sqrt{a/N_{gen}}$, where $a = 0.04$ (according to BABAMC) and N_{gen} is the number of generated events. Including the statistiscal uncertainty in the number of accepted events, we get an error from Monte Carlo statistics of:

$$\frac{\Delta L}{L} = \sqrt{\frac{1}{N_{acc}} + \frac{a-1}{N_{gen}}}$$

In our case the second term is negligible, since $N_{gen} = 1.2{\cdot}10^7$ and $N_{acc} = 271313$.

8 Luminosity Determination using SATR

In order to provide an independent check of the standard luminosity determination, an alternative procedure was developped. It uses the luminosity calorimeter, LCAL, only for the energy measurement, and defines the acceptances with the small angle tracking chamber, SATR.

The most energetic LCAL clusters on the two sides are required to pass the energy thresholds of the standard selection. A fitted track in the tracking chamber must be associated to each of the clusters, one of which must be inside a loose, the other one inside a tight fiducial area of the SATR. The tight fiducial area covers polar angles between 60 and 80 mrad, the loose one those between 57.4 and 85 mrad. In addition, the fitted tracks are both required to have a distance of more than 3 cm from the vertical axis in the plane $z = 280\,\mathrm{cm}$, thus excluding the zone corresponding to the vertical crack in the luminosity calorimeter. Again, the side on which the tight fiducial cut is applied alternates with the event number in order to avoid systematic effects. Furthermore, the acoplanarity of the event is required to be less than 10°.

For the determination of the cross section a Monte Carlo simulation such as described in section 6 is used. The accepted cross section was found to be $(12.58 \pm 0.18)\,\mathrm{nb}$ which, because of the smaller fiducial region, is about one half of that of the standard method.

The track reconstruction efficiency is a critical quantity for the alternative method of the luminosity determination. It is calculated separately from the event counting and the cross section determination. For that purpose, events are selected which contain two back-to-back LCAL clusters well within the SATR acceptance. The track reconstruction efficiency is then determined as the ratio of the number of events with two found tracks to the total number of events. For real data and simulated data, efficiencies of $(90.18 \pm 0.12)\,\%$ and $(95.74 \pm 0.34)\,\%$ respectively were obtained. Thus, the ratio between the track reconstruction efficiencies for real data and Monte Carlo events was found to be 0.9419 ± 0.0036 (statistical errors only).

The list of systematic errors contains contributions from most sources that show up in the standard method. In addition, there is an extra contribution from the systematic error of the ratio of the track reconstruction efficiencies for real data and Monte

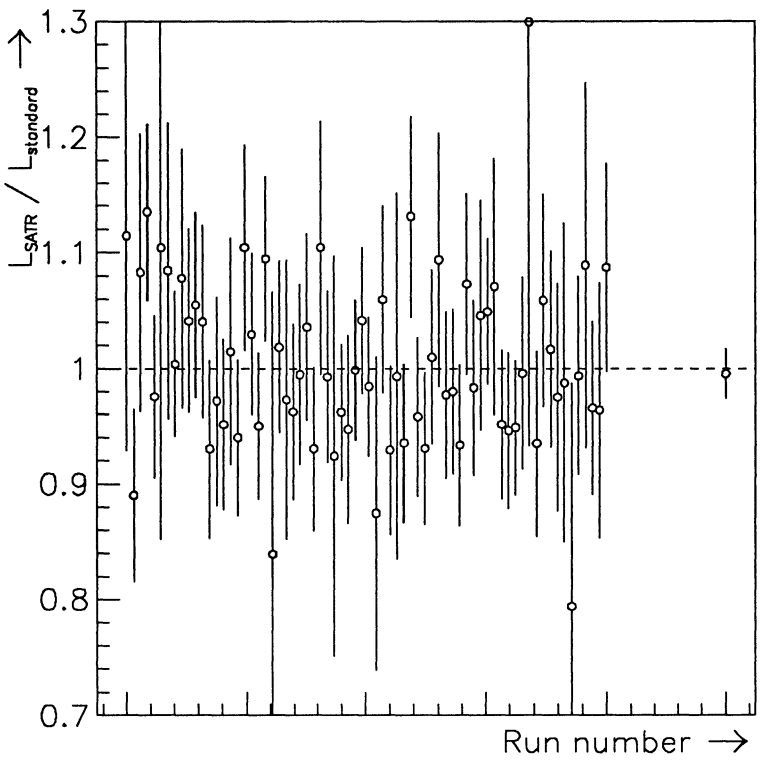

Figure 23: Ratio of alternative and standard luminosity for part of the 1990 data. The data points correspond to one run each. The error bars contain both statistical and systematic errors. In the rightmost bin, the average is shown; its numerical value is 0.995 ± 0.022.

Carlo events. The systematic errors of the alternative luminosity determination are summarized in Table 3. By adding the contributions quadratically, one obtains 1.65 % experimentally. The theoretical error is assumed to be the same as in the standard method.

Source of systematic error	
Background processes	0.001
LCAL energy scale, uniformity, resolution	0.002
Internal alignment, track angular resolution	0.004
External alignment, beam position	0.001
Statistics of MC simulation	0.015
Ratio of track reconstruction efficiencies	0.005
Total experimental uncertainty	0.017

Table 3: Contributions to the systematic error of the alternative method for the luminosity measurement, using SATR to define the acceptance

So far, the alternative method was applied for the determination of the luminosity of about 20 % of the 1990 data. Good agreement between the standard and the alternative method was found. The ratio of the luminosities as determined by the alternative and the standard method was found to be 0.995 ± 0.022, without any dependence on the CMS energy. It is shown as a function of time in figure 23.

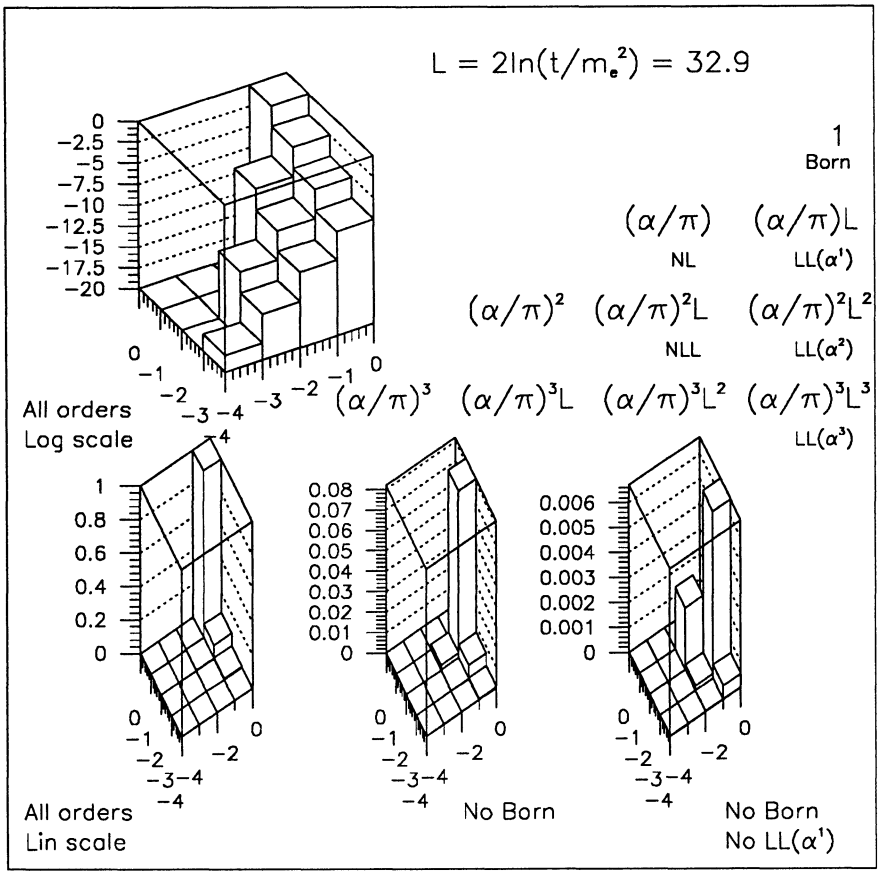

Figure 24: Classification of different contributions to the Bhabha cross–section (see text). The dominant contributions are removed one by one in the lower part.

9 Theoretical predictions

We can classify different terms in QED calculations according to their content of large logarithms. In the case of Bhabha scattering into the LCAL acceptance the large logarithm is L=$2\ln(t/m_e^2) \sim 33$. In Fig. 24 the terms proportional to different powers of L and α are presented. For each power of α the dominant term is called leading-log (LL) and the other terms are called next-to-leading-log (NLL) or non-leading (NL). Those terms discussed in the text are excplicitly marked on Fig. 24. We see that contributions of increasing order decrease exponentially - this is perturbative QED.

We have used the first order Monte Carlo generator BABAMC [3] to calculate the theoretical cross–section for our Bhabha event selection, and we have calculated higher order LL correction to this cross–section. In the following sections we will discuss the precision of BABAMC and the higher order corrections.

9.1 The Monte Carlo generator BABAMC

In the angular region of our measurements the photon t-channel exchange dominates. Photon-Z interference contributes to about $\pm 0.6\%$ at the Z^0 half-width and vanishes both at the Z^0 peak and outside the Z^0 resonance. There is also small, $\sim 0.1\%$, contribution of interference between photon s- and t-channel. BABAMC is a first order generator where all these effects are included.

9.1.1 Precision of BABAMC

In order to check the precision of the first order calculations in BABAMC, we have compared its results to the numerical benchmark of S. Jadach et al. [9] which has a technical precision of 0.02% [2].

In this comparison vacuum polarisation and Z contributions were switched off in BABAMC. The value of the first order correction in BABAMC agreed to better than 0.1% with the benchmark when the k_0 parameter was equal to 0.001 [3]. The result was different by about 0.2% for k_0 equal to 0.01. We have checked that the small difference is due to interference between the s- and t-channel photon exchange which is present in BABAMC, but absent in the benchmark calculation.

Thus, the technical precision of BABAMC with the k_0 equal to 0.001 can be claimed to be better than 0.1%.

9.1.2 Higher order vacuum polarisation corrections

In BABAMC vacuum polarisation is simply added as 2ReΠ ($\sim$+5.3% in ALEPH) in the soft part. A well known procedure called Dyson summation [12] can account for higher order corrections and the result should be applied as a multiplicative factor both in the soft and hard (bremstrahlung) part. Averaged over our acceptance this correction becomes +0.23% in the soft part and -0.37% in the hard part (where the average vacuum correction has been multiplied with the average first order correction). The mean value multiplication may oversimplify the convolution of the vacuum polarisation and the first order correction over the t range of our event selection, so in order to calculate these corrections exactly, we have modified the photon treatment in BABAMC to include Dyson summation[4]. It is important to note that large cancellations exist between the hard and soft parts of the cross–section, and we therefore checked that the k_0 dependence of the BABAMC results is the same before and after changes. We have found that the correction from higher order vacuum polarisation is -0.226 $\pm$0.04% for our experimental cuts, in reasonable agreement with the above mentioned approximate calculation.

9.1.3 Higher order bremsstrahlung corrections - LUMLOG

We have used the generator LUMLOG written by S. Jadach et al. [10] to calculate a higher order bremsstrahlung correction to BABAMC. LUMLOG is a leading-log generator up to $O(\alpha^3)$ with initial state bremsstrahlung only. It was checked against analytical calculations and another Monte Carlo program. In this way a technical precision of $2 * 10^{-4}$ was obtained. The LUMLOG higher order radiative correction to BABAMC for the actual experimental cuts amounts to 0.161$\pm$0.02%, where the error is statistical.

---

[2]The technical precision includes all the errors related to the infrared cut–off, numerical approximations and programming errors, quality of random numbers etc. It can be estimated by comparing two or more independent programs [9,10]. It does not include physics effects like higher order corrections

[3]The infrared cut–off k_0 separates the elastic scattering from the hard bremsstrahlung contribution. We have checked for two different experimental cuts and $k_0 = 0.001$ that the agreement between BABAMC and OLDBAB [11] (the program used in PETRA) is better than 0.01%

[4]We are gratefull to R. Kleiss[13] for helping us to correct the hard bremstrahlung part of the cross-section.

	ALIBABA		LUMLOG
t_{max},L,L-1	3.38	L-1	2.79
t_{min},L,L-1	2.90	L-1	2.34
t_{max},L	4.04	L	3.11
t_{min},L	3.51	L	2.61

Table 4: The higher order correction calculated by the LUMLOG and ALIBABA programs in units of 10^{-3} times the Born cross–section

Δr_{min} fiducial side (cm)	0	+3.0	+3.0	+3.0
Non fiducial margin (cm)	0.5	2.9	3.5	0.9
$O(\alpha^1)$ corr. (%)	-6.8	-6.1	-5.6	-7.7
($LL(\alpha^3)$ - $LL(\alpha^1)$) corr. (%)	+0.161	+0.089	+0.065	+0.208
higher order vac. pol. corr. (%)	-0.226	-0.234	-0.202	-0.332
total (%)	-0.065	-0.145	-0.137	-0.124

Table 5: Dependence of higher order correction on experimental cuts

A comparison between the results of LUMLOG and the luminosity version of the ALIBABA [15] program was made. The ALIBABA results were obtained by W. Beenakker [16]. In order to make this comparison the first-order non-leading part, the Z^0, the vacuum polarisation contributions and the the final state radiation were switched off in ALIBABA. Acceptance cuts similar, but not identical, to the experimental cuts were applied, in order to allow analytical calculations in ALIBABA. Table 4 compares the two programs at the minimum and maximum scattering angle and for two choices of the leading log parameter (L and L-1). It is seen that the differences on the value of the second order correction never exceed 0.1%. Since ALIBABA performs a different calculation, this does not affect the estimated technical precision of LUMLOG.

Final state bremsstrahlung is not included in LUMLOG. This approach is justified by the KLN theorem [17] stating that, since photons collinear with the final state leptons cannot be distinguished experimentally, the LL final state correction vanishes. The non-leading $O(\alpha^1)$ correction is included in BABAMC. The next-to-leading $O(\alpha^2)$ correction is included in the error estimate in Table 7. More discussion can be found in Ref. [10].

9.1.4 Dependence of higher order correction on experimental cuts

We have calculated both the higher order bremstrahlung correction and the higher order vacuum polarisation correction for different geometrical cuts in the detector. The results are presented in Table 5.

The first column represents corrections for standard ALEPH cuts. The others had the fiducial side acceptance reduced by one pad size (3 cm). In all cases the margin

LL(α^3) - LL(α^1) (sec.9.1.3)	+0.161±0.02%
higher order vac. polarisation (sec.9.1.2)	-0.226±0.04%
total correction to BABAMC	-0.065±0.05%

Table 6: Corrections to BABAMC

NLL(α^2) QED bremsstrahlung	0.2%
l^+l^- pair production	0.1%
vacuum polarisation	0.08%
technical precision of BABAMC (sec. 9.1.1)	0.1%
corrections to BABAMC (Table 6)	0.05%
technical precision of LUMLOG (sec. 9.1.3)	0.02%
knowledge of ALEPH cuts (sec. 9.1.4)	0.1%
total theoretical error	0.3%

Table 7: Contributions to the theoretical error

between the non fiducial and fiducial side is given for the region closest to the beam and having the highest counting rate. We see that when we change the acceptance both corrections change more than their sum. We obtain this partial cancellation because both corrections are proportional to the $O(\alpha^1)$ correction in Table 5 and have opposite signs.

We have calculated all these corrections at particle level. Some of the quantities used for cuts are smeared by the detector, especially the non fiducial margin. Since the maximum shift in the non fiducial margin going from particle level to detector level amounts to 3mm, the error from detector smearing of 0.1% in Table 7 is conservative.

9.2 Higher order QED correction to luminosity measurement and its total error

Table 6 lists our corrections to the O(α) QED calculation of BABAMC.

The errors in Table 6 come from the limited MC statistics or are related to the precision of our changes to BABAMC needed to calculate the higher order vacuum polarisation contribution. Different contributions to the total error of theoretical prediction of luminosity in ALEPH are summarised in Table 7.

The following comments should be made. The first two contributions describe the error due to physics not included in the present calculations and come from the paper of Jadach et al. [10] . The error on the hadronic vacuum polarisation was calculated on the basis of a paper by Burkhardt et al. [18]. Finally, since the errors are independent, we have added them quadratically.

10 Conclusion

Table 2 shows the experimental systematic errors on the luminosity in 1990. The error from each potential source is conservatively estimated as the maximum observed variation due to a change in a relevant cut. The theoretical errors are listed in Table 7. Added quadratically the errors become in total 0.6% (experimental) and 0.3% (theoretical).

11 Acknowledgements

Progress in the theoretical calculations of the Bhabha cross–section was possible thanks to discussions with S. Jadach, E. Richter-Wąs, B.F.L. Ward and Z. Wąs. Comparisons with ALIBABA calculations have been made in collaboration with W. Beenakker. R. Kleiss has helped us implement the higher order vacuum polarisation in BABAMC.

References

[1] "Measurement of Electroweak Parameters from Z decays into Fermion Pairs", Zeitschrift für Physik C (1990) 365-391.

[2] D.Decamp et al. (The ALEPH Collaboration)
Nuclear Instruments and Methods A294 (1990) 121-178.

[3] M.Böhm, A.Denner and W.Hollik, Nucl.Phys. B304 (1988) 687,
F.A Berends, R.Kleiss and W.Hollik, Nucl.Phys. B304 (1988) 712,
Computer program BABAMC, courtesy of R.Kleiss.

[4] H.Burkhardt et al., Z. Phys. C43 (1989) 497.

[5] D.Y.Bardin et al.: Monte Carlo group in
"Proceedings of the Workshop on Z Physics at LEP",
CERN Report 89-08.

[6] H.Meinhard, Thesis January 1991.

[7] L.Mirabito, Thesis February 1991.

[8] J.Wear, Thesis April 1991.

[9] S.Jadach, E.Richter-Was, Z.Was and B.F.L.Ward, Phys. Lett. B252 (1991) 469.

[10] S.Jadach, E.Richter-Was, Z.Was and B.F.L.Ward, CERN-TH5995 preprint, to be published in Phys. Lett.

[11] F. A. Berents and R. Kleiss, Nucl. Phys. B228 (1983) 537.

[12] F. Halzen and A. D. Martin, "Quarks and Leptons", 1984, ed. by John Wiley and Sons, Inc., New York, section 7.8 .

[13] R. Kleiss, private communication.

[14] W.Beenakker, F.A.Berends and S.C. van der Marck, Leiden preprint, November, 1990.

[15] W.Beenakker, private communication.

[16] T. D. Lee and M. Nauenberg, Phys. Rev. 133 (1964) 1549; T. Kinoshita, J. Math. Phys. 3 (1962) 650.

[17] H.Burkhardt F. Jegerlehner, G. Penso and C. Verzegnassi, Z. Phys. C43 (1989) 497.